

The Swarm Langmuir Probe Ion Drift, Density and Effective Mass (SLIDEM) Product

Ivan Pakhotin (✉ pakhotin@ualberta.ca)

University of Calgary <https://orcid.org/0000-0001-6872-9146>

J. K. Burchill

University of Calgary

M. Förster

Helmholtz-Zentrum Potsdam GFZ: Deutsches Geoforschungszentrum Potsdam

L. Lomidze

University of Calgary

Full paper

Keywords: Plasma density, ionospheric composition, ionospheric convection, Langmuir probe, ionosphere, space weather

Posted Date: February 9th, 2022

DOI: <https://doi.org/10.21203/rs.3.rs-1322241/v1>

License: © ⓘ This work is licensed under a Creative Commons Attribution 4.0 International License.

[Read Full License](#)

1 **The Swarm Langmuir Probe Ion Drift, Density and Effective Mass (SLIDEM) Product**

2 I. P. Pakhotin^{1*}, J. K. Burchill¹, M. Förster^{2,3}, L. Lomidze^{1,4}

3 ¹ Department of Physics and Astronomy, University of Calgary, Calgary, Alberta, Canada

4 ² German Research Centre for Geosciences, Helmholtz Centre Potsdam, Potsdam, Germany

5 ³ Max Planck Institute for Solar System Research, 37077 Göttingen, Germany

6 ⁴ E. Kharadze Georgian National Astrophysical Observatory, Abastumani, Georgia

7 *corresponding author, e-mail: pakhotin@ualberta.ca

8 **Key Points**

- 9 - A new data product for Swarm along-track ion drift velocity, density and effective mass has
10 been derived
- 11 - The addition of faceplate current to ion admittance enables a refinement to Swarm ion
12 density
- 13 - The estimations have been validated against a variety of independent measurements and
14 empirical models

15 **Abstract**

16 Current methods for estimating ion density on Swarm rely on the assumption of 100% O⁺ and
17 no along-track ion velocity flows. These assumptions are routinely violated, particularly on the
18 nightside and during high-latitude and polar cap traversals, compromising the accuracy of the
19 measurements. The use of faceplate current data along with the Langmuir probe ion
20 admittance measurements, and orbital-motion limited (OML) theory, make it possible to relax
21 some of the assumptions inherent in current ESA Swarm density estimates. This further yields
22 along-track ion drift and effective ion mass estimates. This paper describes the theoretical basis
23 for estimating revised ion density, providing a new estimate for effective ion mass, as well as an
24 alternative way of estimating along-track ion drift. The complete Swarm historical dataset has
25 been generated and validated using empirical models (International Reference Ionosphere (IRI-
26 2016), and Weimer (2005)), as well as ground-spacecraft conjunctions. Case studies and
27 statistical results reveal clear geophysical signatures in the new product of light ions at low- and
28 mid-latitudes and along-track ion drift at high latitudes, and their response to space weather.

29 **Keywords**

30 Plasma density, ionospheric composition, ionospheric convection, Langmuir probe, ionosphere,
31 space weather

32

1. Introduction

33 Accurate measurements of key ionospheric parameters such as density, ion species
34 composition, and ion flows, are of crucial importance in studies of Magnetosphere-Ionosphere
35 Coupling (MIC) and determine the dynamics of magnetosphere-ionosphere-thermosphere
36 energy transfer. In particular, the auroral zone is known to be a key interface where energy and
37 momentum is transferred between the two systems at a range of spatio-temporal scales. As ion
38 velocities are routinely used to estimate electric fields via $\mathbf{E} = -\mathbf{v} \times \mathbf{B}$ (e.g. Knudsen et al. 2017,
39 Pakhotin et al., 2018), accurate measurements of these flows allow for better understanding of
40 electromagnetic transverse disturbances, in the form of both Alfvén waves and field-aligned
41 currents (FACs), which provide the basis of the magnetosphere-ionosphere interface. While
42 models such as the Weimer (2005) electric field empirical model, and ground radar
43 observations such as SuperDARN (Greenwald et al., 1995) can estimate convection flows, they
44 inherently focus on larger spatial and temporal scales. Meanwhile recent works (e.g. Codrescu
45 et al., 1995, Rother et al., 2007, Pakhotin et al., 2018, 2020, 2021, Verkhoglyadova et al., 2017,
46 2018) demonstrate that small- and meso-scale disturbances can be responsible for a significant
47 total portion of the energetics of MIC. These scales are inherently going to be missed by both
48 large-scale empirical models and by ground radar-based measurements, and require in-situ
49 observations by satellites such as Swarm sampling at ≤ 1 Hz frequencies.

50 The primary method for measuring ion flows on Swarm is using the Thermal Ion Imager (TII)
51 (Knudsen et al., 2017). Despite periods of degraded data quality arising from residual water
52 vapour and spacecraft-plasma interactions, a robust cross-track ion velocity dataset has been
53 established (Lomidze et al., 2019, 2021, Koustov et al., 2019) and has been utilized in scientific
54 studies including long-duration statistical Poynting flux studies (e.g. Pakhotin et al., 2021).
55 Estimating the along-track component of ion drift is inherently more challenging, and to date a
56 reliable along-track ion drift dataset is unavailable (Knudsen et al., 2017, Burchill and Knudsen,
57 2020). Clearly there is a need for reliable estimates of this component for the full 3D vector to
58 be reconstructed.

59 One aim of this paper is to detail an alternative method for measuring ion along-track flow
60 component at high latitudes, utilizing orbital-motion limited (OML) theory (Mott-Smith and
61 Langmuir, 1926) and the faceplate current measurement, as well as Langmuir probe ion
62 admittance. Since the ion velocity measurement is obtained using a different methodology, it is
63 immune from some of the caveats associated with the classic TII measurement, and as such,
64 forms a valuable addition to the Swarm data product family.

65 The low latitude ionosphere, meanwhile, is dominated by a range of density perturbations and
66 changes associated with, for example, equatorial plasma bubbles (Woodman and La Hoz, 1976),
67 equatorial plasma fountains (e.g. Balan and Bailey, 1995), the Sq current system (e.g.

68 Vasyliunas, 2012), Appleton anomaly (Appleton, 1946), and others. Typically, these phenomena
69 are not associated with strong drifts, but are heavily dependent on density and ionospheric
70 composition. Studies of near-equatorial Alfvén waves, in the form of field-line resonances, and
71 interhemispheric Poynting flux transfer as e.g. MSTIDs (Park et al., 2016), as well as space
72 weather dynamics such as ring current evolution (e.g. Ganushkina et al., 2015), also depend on
73 accurate low-latitude estimations of density and ion composition. Ideally, the composition of
74 individual ions would be measured directly by means such as mass spectrometry. Swarm does
75 not have such instruments on board, and in addition there are known sensitivity issues with
76 mass spectrometers which may prevent them from observing accurate ion composition of cold
77 or warm plasma. Instead, the Swarm Langmuir probe Ion Density and Effective Mass (SLIDEM)
78 methodology allows for the determination of an ion fraction, which is a parameter that is
79 sensitive to the presence of light ions. As such, even small (<5%) deviations from 100% O⁺ at
80 low latitudes may be observed using this method.

81 Swarm ion densities are typically estimated from admittance using a simplified form of OML
82 theory equations, where density is calculated directly from ion admittance signal via

$$83 \quad N_i = \frac{d_s v_s m_s}{2e^2 \pi r_p^2} \quad (1)$$

84 where N_i is the ion density, d_s is the ion admittance (the response of the Langmuir probe
85 current to changes in the bias voltage, $d_s = \frac{\partial I}{\partial V_b}$), v_s is the plasma speed in the ram direction,
86 m_s is the effective (or reduced) ion mass, e is the elementary charge, and r_p is the spherical
87 Langmuir probe radius. In calculating the density in this manner, typically two assumptions are
88 made: first, that the effective ion mass is 16 atomic mass units (AMU), i.e. that the surrounding
89 plasma is 100% singly charged oxygen ions. The second assumption is that the plasma ram
90 speed v_s is equal to the satellite speed, ~7.6 km/sec on Swarm A; in other words, no along-track
91 ion drifts are assumed. As it is known that significant amounts of lighter ions e.g. H⁺ are present
92 particularly on the nightside and at higher altitudes where Swarm B is located (e.g. Smirnov et
93 al., 2021), and also that strong ion drifts are present in both along-track and cross-track
94 directions in the auroral zone, it is reasonable to expect that both of these assumptions are
95 routinely violated, compromising the density estimates. Recent studies revealed that the
96 Swarm LP ion densities are overall 20-35 % lower compared to their independent
97 measurements (Lomidze et al., 2018, 2021; Larson et al., 2021).

98 By introducing the faceplate current measurement, it is possible to refine the density
99 estimation while relaxing the above assumptions, resulting in more accurate estimations of this
100 parameter. In addition, this approach may also yield either the effective ion mass, or the along-

101 track ion velocity, depending on the latitude. The remaining parameter must then be
102 estimated.

103 The methodology we propose here uses the known lack of significant along-track ion drifts at
104 low to middle magnetic latitudes and consequently assumes the along-track ion velocity in
105 those regions to be zero (co-rotating velocity does not impact the along-track component).
106 Then, effective ion mass and density may be derived, from which the fraction of light ions may
107 be estimated. However, at high latitudes, we must estimate the effective ion mass from e.g. an
108 empirical model to derive along-track ion velocity. Since we no longer rely on the assumption of
109 zero velocity, we expect more realistic ion density estimates. The three parameters obtained in
110 this manner are validated against estimates from empirical models, primarily using the
111 International Reference Ionosphere 2016 or IRI-2016 (Bilitza et al., 2016, Truhlik et al., 2015) for
112 effective ion mass and density comparisons, and the Weimer (2005) electric field model for
113 along-track ion drifts.

114 The rest of the paper is structured as follows. Section 2 presents the OML equations and Swarm
115 measurement details, as well as outlining the empirical models. Section 3 presents case studies
116 and statistical examples of the SLIDEM products and validation datasets, while Section 4
117 discusses the validity of the products. Section 5 summarises the paper.

118 **2. Data and Methodology**

119 In this Section the theoretical basis for estimating along-track ion drift and effective ion mass
120 from the Swarm measurements and an empirical high-altitude ion composition model is
121 introduced. Empirical models and incoherent scatter radar data used for data validation are
122 described.

123 **Swarm measurements and OML equations**

124 The Swarm mission (Friis-Christensen et al., 2006) was launched in 2013 into a low-Earth polar
125 orbit. In the main science phase, Swarm A and C fly side by side with a 1.4 degree cross-track
126 separation at the equator and a varying along-track separation, typically ~10 sec, at an altitude
127 of ~450 km in the beginning of the main science phase. Meanwhile, Swarm B orbits ~60 km
128 higher, with its local time typically different from that of Swarm A/C. The spacecraft are
129 equipped with the 50 Hz Vector Field Magnetometer (Jørgensen et al., 2008) as well as Thermal
130 Ion Imagers to obtain ion velocity drifts at up to 16 Hz, a pair of Langmuir probes to obtain ion
131 density and electron temperature estimates at 2 Hz, and a planar fixed-bias probe (“faceplate”)
132 for current measurements at 16 Hz (Knudsen et al., 2017).

133 The Langmuir probes operate >99% of the time in what is known as the Harmonic Mode
134 (Knudsen et al., 2017). This allows them to sample electric current and admittance parameters

135 for three separate regions of the Volt-Ampere characteristics: “ion”, “linear electron” and
 136 “retarded electron”. For the purposes of this paper we use only the ion admittance, which, for a
 137 straightforward OML approximation, is given by (Knudsen et al., 2017)

$$138 \quad d_i = \frac{\partial I}{\partial V_b} = \frac{2N_i e^2}{M_{eff} v_i} \pi r_p^2 \quad (2)$$

139 where d_i is the ion admittance, I is probe current, and V_b is the applied bias. As the right-most
 140 side of equation (2) indicates, the ion admittance is a function of ion density N_i , effective ion
 141 mass M_{eff} , and ion ram velocity v_i , as well as Langmuir probe radius r_p , and ion net charge,
 142 assumed to be the elementary charge e . The ESA Level 1b density estimate uses this equation,
 143 assuming a 100% O+ ionosphere ($M_{eff} = 16$ A.M.U.) and no along-track ion drifts such that $v_i =$
 144 ~ 7.6 km/sec is the satellite speed.

145 Because the ion admittances of individual ion species sum in proportion to their relative
 146 concentrations, the effective ion mass in the above equation, in contrast to average mass, is
 147 equal to the reciprocal of the reciprocals of the constituent species:

$$148 \quad \frac{1}{M_{eff}} = \frac{1}{N_i} \sum_{s=1}^k N_s \frac{1}{m_s} \quad (3)$$

149 where m_s is the mass of the s -th ion species. It is also referred to as reduced mass. A feature of
 150 this parameter is that it is much more sensitive than average mass to small amounts of light
 151 ions. For example, even a 10% H+ fraction will reduce this value from 16 AMU to 6.4 AMU. It
 152 can be seen that in this scenario the density obtained under a 100% O+ assumption
 153 dramatically overestimates the true ion density. This effect is expected to be particularly strong
 154 on the nightside where higher concentrations of light ions can be present.

155 Similarly, the assumption of zero along-track ion drift can fail in the auroral zones where ion
 156 drifts of up to several km/s are not uncommon (e.g. Lomidze et al., 2019, Archer et al. 2017). As
 157 such it can be seen that both of the assumptions used in calculating ion density are expected to
 158 be routinely violated.

159 One solution to this problem is to bring in current measurements from the EFI faceplate.
 160 Neglecting the effects of plasma sheath, and assuming all ions have a single charge and flow at
 161 the same speed, the current collected by the frontal faceplate is

$$162 \quad I_{FP} = -N_i e v_i A_{FP} \quad (4)$$

163 where A_{FP} is the faceplate area (804 cm²). Equation (4) may be combined with equation (1) to
 164 obtain revised expressions for high-latitude ion density N_i

$$165 \quad N_i = \sqrt{\frac{-d_i I_{FP} M_{eff}}{2e^3 A_{FP} \pi r_p^2}} \quad (5)$$

166 and along-track ion drift

$$167 \quad v_i = v_{sat} - \sqrt{\frac{-2e\pi r_p^2 I_{FP}}{d_i A_{FP} M_{eff}}}. \quad (6)$$

168 The effective ion mass must still be assumed; for this study we use the IRI 2016 high-altitude
 169 ion composition model (Truhlik et al. 2015) to calculate an empirical effective ion mass based
 170 on four ion species (O+, N+, He+, and H+).

171 Similarly, at low-to-mid-latitudes the along-track ion drift may be neglected in comparison with
 172 the satellite speed, yielding

$$173 \quad m_{eff} = \frac{-2e\pi r_p^2 I_{FP}}{d_i A_{FP} v_{sat}^2} \quad (7)$$

174 One limitation of this approach is that the Swarm faceplate current measurements have been
 175 found to be reliable only when the faceplate voltage is set to -3.5 V, whereas the TII science
 176 operations are conducted with faceplate voltage of -1 V (Knudsen et al., 2017). SLIDEM product
 177 measurements are therefore available only when the faceplate voltage is set to -3.5 V,
 178 amounting typically to several orbits per day until mid 2018. Swarm TII operations have
 179 required setting the faceplate voltage to -1 V increasingly often in recent years, reducing the
 180 availability of SLIDEM products. A notable exception was that the faceplate was operated at $-$
 181 3.5 V almost continuously on Swarm C from mid 2019 to mid 2020. It should be noted that
 182 plasma sheath effects modify the effective areas of both the frontal faceplate and the Langmuir
 183 probe, such that they are not equal to their physical areas. For the faceplate, Particle-In-Cell
 184 simulations indicated that a correction factor for the effective area is required (Resendiz Lira et
 185 al., 2019):

$$186 \quad \delta_{FP} = \frac{\alpha P \lambda_D}{A_{FP}} \left(1 - \frac{eV}{\frac{1}{2} M_{eff} v_{\perp}^2} - \beta \frac{eV}{kT_e} - \frac{\gamma}{eV} \frac{e^2}{4\pi\epsilon_0\lambda_D} \right) \quad (8)$$

187 where $\lambda_D = \left(\frac{\epsilon_0 k T_e}{e^2 n}\right)^{1/2}$ is Debye length, k is the Boltzmann constant, T_e is electron temperature,
 188 V is potential (spacecraft floating potential plus faceplate bias), ϵ_0 is the permittivity of free
 189 space, $\alpha=0.06929$, $\beta=0.11552$, $\gamma=66.0913 \times 10^6$ are fitting parameters. This δ_{FP} term may be
 190 applied in place of A_{FP} e.g. $A_{eff} = A_{FP} * (1 + \delta_{FP})$.

191 Meanwhile the Langmuir probe cross section is also modified by the plasma sheath effects;
 192 however, the geometry is more complex. As per (Resendiz Lira and Marchand, 2021), since the
 193 probe is positioned near the negatively charged satellite body, lighter ions are preferentially
 194 deflected towards the satellite rather than towards the detector. As such, depending on ion
 195 composition, the effective area is generally smaller than the physical area. The equation is as
 196 follows:

$$197 \quad \delta_{LP} = \alpha \frac{\lambda_D}{r_p} \left(1 - \beta \frac{eV_f}{\frac{1}{2} M_{eff} v_d^2} - \gamma \frac{eV_f}{kT_e} \right) - \zeta V_f + \xi$$

(9)

198 where $\alpha=7.996 \times 10^{-3}$, $\beta= 5.431$, $\gamma= 0.2191$, $\zeta=5.915e-3 / V$ and $\xi=-1.743e-2$. This correction
 199 factor is applied to probe area, $\pi r_p^2 * (1 - \delta_{LP})$. Thus the corrected form of equation (5) becomes:

$$200 \quad v_i = v_{sat} - \sqrt{\frac{-2e(1 - \delta_{LP})\pi r_p^2 I_{FP}}{d_i(1 + \delta_{FP})A_{FP}M_{eff}}}$$

(10)

201 For the frontal faceplate, the effective area is generally larger than the physical area, while for
 202 the Langmuir probe, the effective cross-sectional area is generally smaller than the physical
 203 cross-sectional area. It can be seen then, that for both velocity and effective ion mass, the
 204 combined effects of the Langmuir probe and frontal faceplate plasma corrections generally act
 205 to make the numerator smaller and the denominator larger, i.e. to decrease both quantities.
 206 Meanwhile the corrected density equation would be:

$$207 \quad N_i = \sqrt{\frac{-d_i I_{FP} M_{eff}}{2e^3 A_{FP} (1 + \delta_{FP}) (1 - \delta_{LP}) \pi r_p^2}}$$

(11)

208

209 For equation (11), then, the correction terms somewhat counterbalance each other, since both
 210 are located in the denominator.

211 Provision has been made for post-processing the SLIDEM along-track ion drift to detrend
212 slowly-varying offsets across the polar regions. Mid-latitude drift, which can be several km/s in
213 the raw estimates, are thereby zeroed at poleward quasidipole latitudes between 50 and 51
214 degrees. This approach is similar to the one used for the cross-track flow dataset (Koustov et
215 al., 2019; Lomidze et al., 2019; Burchill and Knudsen, 2020).

216 **Weimer 2005 Empirical Convection Electric Field Model**

217 The Weimer 2005 electric field model is an empirical electric potential and field model for the
218 northern and southern hemisphere high-latitude regions, derived from DE-2 data between
219 1981 and 1983 (Weimer, 2005). This model uses spherical harmonic fitting to obtain convection
220 cell mapping as a function of solar wind parameters such as IMF B_y , IMF B_z , solar wind speed,
221 solar wind density, and AL Index. Recently, the Swarm TII cross-track ion velocity flows were
222 validated against the Weimer (2005) model by Lomidze et al. (2019, 2021), who showed good
223 statistical agreement between the two, similar large-scale median flow patterns, and examples
224 of matching data for individual polar orbits. The methodology of Lomidze et al. (2019) is
225 adapted to the present study to assess the validity of the SLIDEM along-track ion drift
226 estimates. While the Weimer 2005 model is not generally expected to reproduce flows on a
227 measurement-by-measurement basis, it is believed to be reliable when predicting gross
228 features for relatively steady ionospheric conditions.

229 **International Reference Ionosphere**

230 The International Reference Ionosphere is a joint effort between COSPAR and URSI to obtain an
231 international standard of key ionospheric parameters (Bilitza et al., 2017). The SLIDEM product
232 includes empirical estimates of effective ion mass based on the latest high-altitude (>350 km)
233 IRI ion composition model (Truhlik et al., 2015), which provides relative ion concentrations of
234 O^+ , N^+ , He^+ , and H^+ . Although this model is not intended to reproduce Swarm measurements
235 point-by-point, it serves as a solid basis for demonstrating expected trends in effective ion
236 mass, and it is expected to be more reliable at high latitudes for the ion density and drift
237 estimates than assuming pure O^+ . The IRI 2016 model is also used to obtain electron and ion
238 temperatures and electron densities for product validation. The IRI is used here as a common
239 reference to compare SLIDEM with respect to the existing L1b product, particularly to
240 investigate the hypothesis that light ions on the nightside lead to significant errors in density
241 when assuming pure O^+ . It is noted that there is compelling evidence that IRI significantly
242 overestimates topside ionospheric density (Bilitza and Xiong, 2021), particularly during low
243 solar flux conditions. Thus, we expect both SLIDEM and L1b to systematically show lower
244 ionospheric densities compared with IRI.

245 **Incoherent Scatter Radar**

246 A set of seven overflights (conjunctions) by Swarm A of several incoherent scatter radar
247 facilities (Evans, 1969) was identified to validate the measured faceplate current and ion
248 admittance. The radar sites were chosen to cover equatorial (Jicamarca), middle (Millstone Hill)
249 and high latitudes (EISCAT-Tromso). For each radar, one dayside and one nightside conjunction
250 was identified. In addition, a second nightside conjunction was identified between Swarm A and
251 Jicamarca, where the floating potential of Swarm A recorded an unusually low value (-8.42 V),
252 to investigate whether this would invalidate the SLIDEM methodology.

253 For each of the seven conjunctions, values for electron density and electron temperature have
254 been obtained separately from the ground radar, from the Swarm satellite itself (using the
255 Swarm SITE product (Lomidze et al., 2021)), and from IRI-2016. In addition, relative ion
256 composition for H⁺, He⁺, N⁺, and O⁺ was obtained from IRI-2016. From these parameters the
257 theoretical faceplate current and ion admittance have been estimated using the empirical
258 correction models of Resendiz Lira et al. (2019) and Resendiz Lira and Marchand (2021), and the
259 results are compared with the Swarm A measured faceplate current and high-gain probe ion
260 admittance.

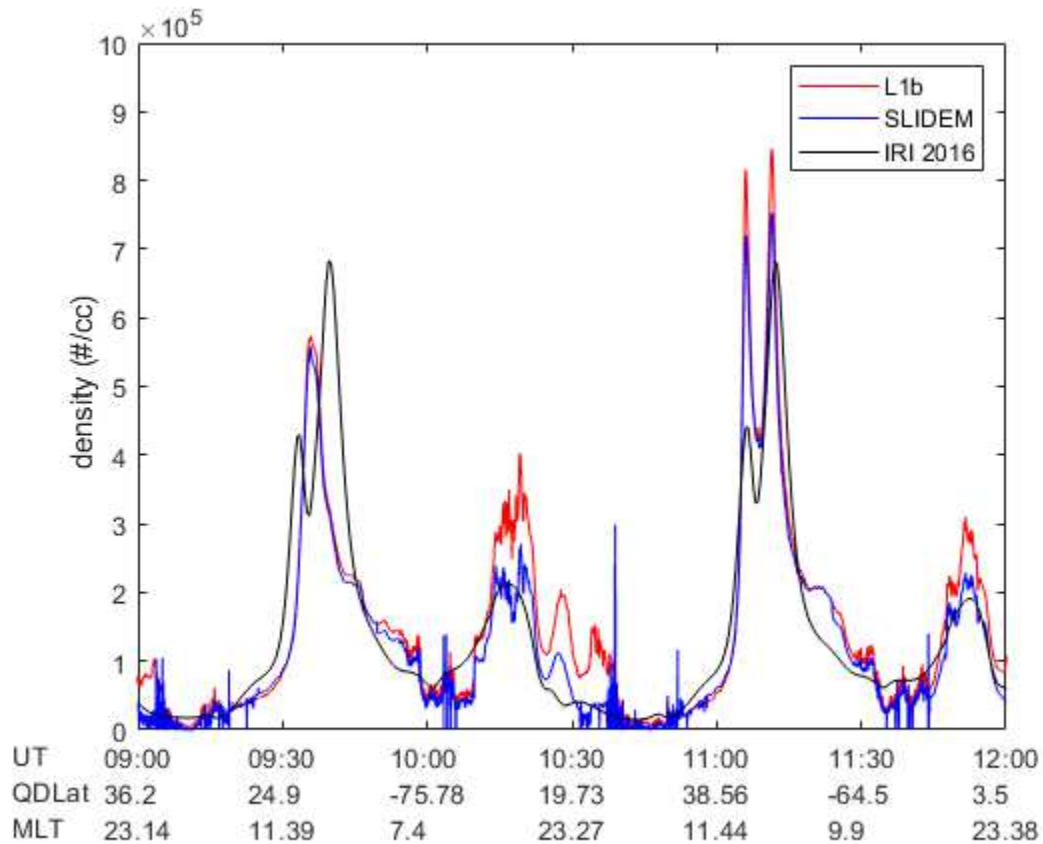
261 **3. Results**

262 This section presents statistical and time series data for the three primary outputs: ion density,
263 effective ion mass, and the along-track component of ion drift. Intervals of data were chosen on
264 the timescales of days to months in order to both demonstrate robustness of the results and to
265 capture both seasonal and orbital variability. In particular, each Swarm orbit drifts on the
266 timescale of months such that the ascending orbital track changes from the dayside, through
267 dawn-dusk, to the nightside. For effective ion mass and density, the magnetic quasi-dipole (QD)
268 argument of orbit parameter is used in place of latitude, where +180 degrees is added to QD
269 latitude values on the descending orbit track. This allows both the dayside and nightside tracks
270 to be displayed on a single plot, showing differences in plasma density and effective ion mass
271 day/night variation. The SLIDEM product generates effective ion mass estimates around the
272 entire orbit, but measurements are flagged as valid only for quasi-dipole latitudes equatorward
273 of ± 50 degrees. Ion drift is estimated only at quasi-dipole latitudes poleward of ± 50 degrees.

274 **Density**

275 An example of the time series of the density estimates obtained from SLIDEM (blue), from the
276 existing ESA Level 1b product (red), and from the IRI model (black), is displayed in Figure 1.
277 Density variations with latitude are correctly captured by the SLIDEM on the dayside and on the
278 nightside. The dayside ionosphere exhibits higher densities, in line with expectations as this is
279 the side exposed to EUV radiation. The nightside equatorial regions is where the difference
280 between the two Swarm products is most pronounced. Since the nightside ionosphere may

281 contain a higher fraction of light ions, its effective ion mass can be significantly different from
 282 the assumed 16 A.M.U. As such, SLIDEM is expected to exhibit an improved nightside
 283 ionosphere density estimation performance. It shows lower disagreements when compared
 284 with IRI, while the Level 1b product can be larger than IRI-2016 nightside densities by ~50%, as
 285 can be seen at 10:20 UT and at 11:50 UT in Figure 1.



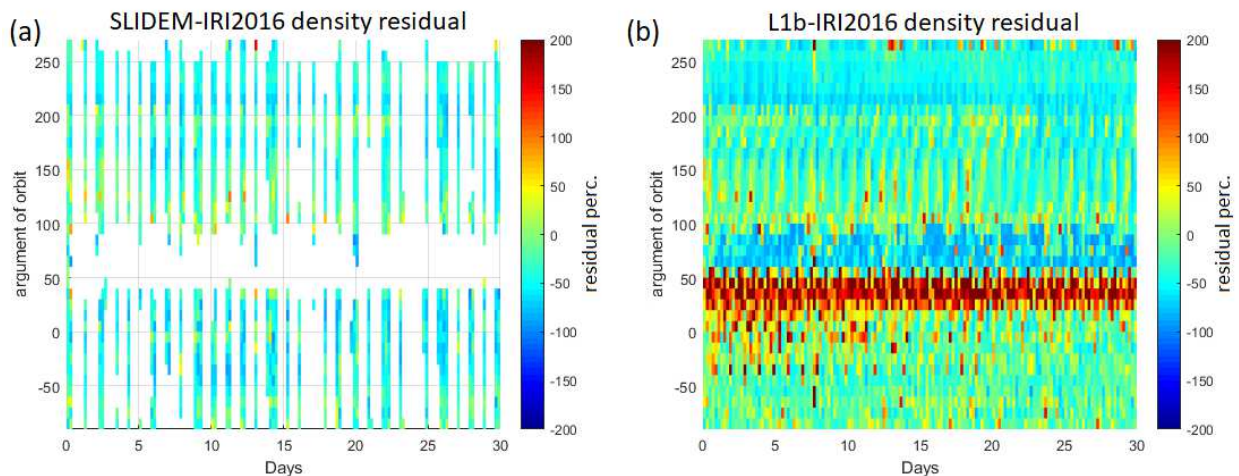
286

287 **Figure 1: Swarm A density estimations for 1 January 2018, using the SLIDEM methodology, the existing Level 1b estimate,**
 288 **and an independent measurement from IRI-2016.**

289

290 To examine longer time series, residuals are calculated by subtracting the densities obtained by
 291 SLIDEM from those obtained from IRI, as percentages of the IRI density values. The same is
 292 done for the Level 1b product to obtain residuals for that scenario. Both residuals are divided
 293 by IRI-2016 values to obtain relative percentage residuals, which are then plotted in Figure 2 as
 294 a function of time and magnetic quasi-dipole argument of orbit. The streaks of white
 295 background in the left-hand panel indicate unavailability of data. From Figure 2 it can clearly be
 296 seen that the Level 1b product (right-hand panel) routinely returns higher nightside densities
 297 compared with IRI. The improved agreement for the SLIDEM product (left-hand panel) is clear

298 particularly with respect to overestimation, although both in-situ measurements show lower
 299 densities than IRI at systematic intervals, similar to Bilitza and Xiong (2021). For the time
 300 interval displayed in Figure 2 the mean of the absolute of the residual between SLIDEM and IRI
 301 (Figure 2 (a)) is 43.9% (similar to the 42% bias for NeQuick topside option within IRI as detailed
 302 in Bilitza and Xiong, 2021), while that between the existing Level 1b density product and IRI
 303 (Figure 2(b)) is 55.2%. Note, only those L1b-IRI2016 residual elements where data existed for
 304 SLIDEM-IRI2016 residuals were used in calculating the above values. The additional residual
 305 within L1b, beyond that expected for IRI/spacecraft comparisons, is believed to be due to the
 306 significant differences on the nightside due to effective ion mass deviating from 16 AMU. The
 307 SLIDEM methodology removes this assumption, yielding lower nightside residuals when
 308 compared with IRI-2016. A comparison between the SLIDEM and L1b densities (not shown)
 309 indicates the overall median difference of 17.3 % but with noticeably larger L1b values on the
 310 nightside.

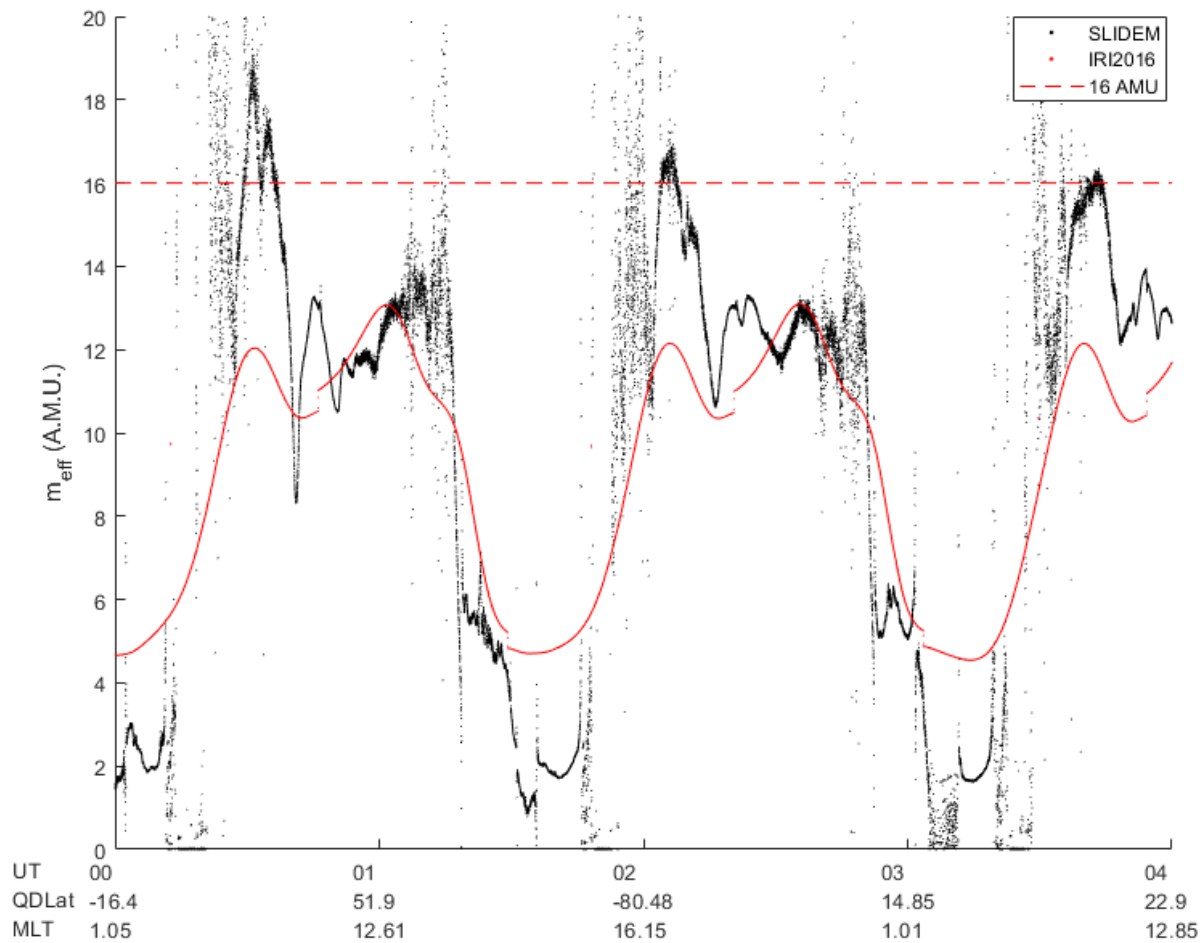


311
 312 **Figure 2: Statistical analysis of the residual of density estimates between SLIDEM (IDM) and IRI-2016, as well as Level1b and**
 313 **IRI, for the time period 1-30 January 2018. Gaps in (a) denote periods of missing SLIDEM data coverage. Residuals are in units**
 314 **of percentage of the total density.**

315 **Effective Ion Mass**

316 The effective ion mass time series for a representative time period are displayed in Figure 3. It
 317 can be seen that, as Swarm traverses from dayside to nightside, the increasing fraction of light
 318 ions such as H⁺ decreases the effective ion mass to values much lower than 16 A.M.U. (red,
 319 dashed line). This is evidenced both by the IRI-2016 model (red) and SLIDEM observations
 320 (black). The SLIDEM effective ion mass estimates are not expected to be generally valid at
 321 higher latitudes as the spacecraft enters the auroral zone, since along-track ion velocity may no
 322 longer be neglected. Nevertheless, at lower latitudes the agreement is good and small-scale
 323 features, as well as variations between consecutive orbits, are present in both the IRI-2016 and

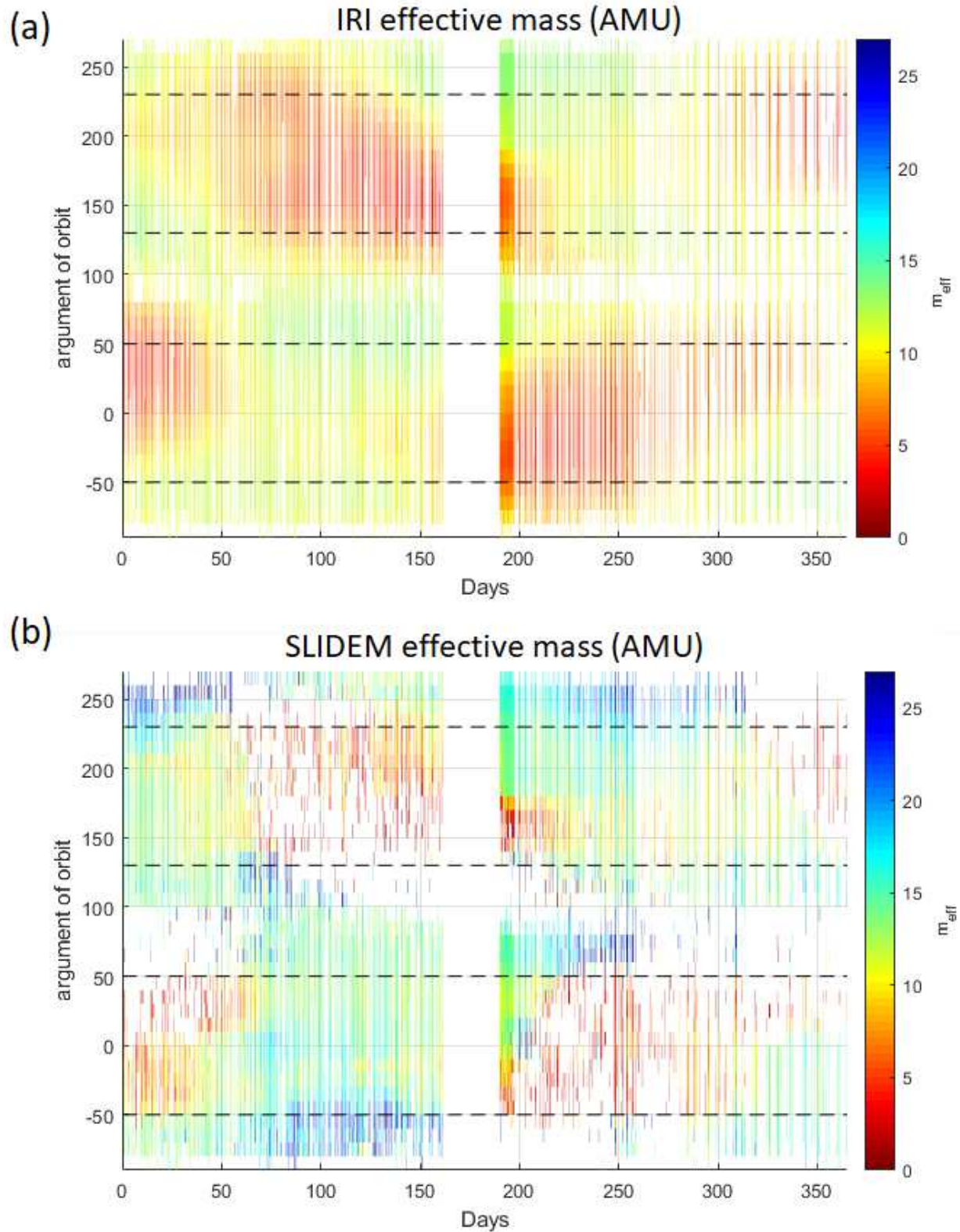
324 SLIDEM data. The SLIDEM estimate not unexpectedly shows more structure than the IRI model.
 325 All measurements are here plotted irrespective of quality flags to illustrate the range of
 326 variability and possible quality issues, such as effective ion mass occasionally falling below 1
 327 AMU.



328

329 **Figure 3: Swarm A effective ion mass estimation using SLIDEM and IRI-2016 for a representative time period (1 May 2018).**
 330 **Data is shown for the entire orbit period, including times when significant along-track ion drifts are present.**

331 The effective ion mass estimates may be plotted against argument of orbit and time, as shown
 332 in Figure 4 for one full year (2018). It can be seen that as the Swarm orbit drifts, the areas of
 333 low effective ion mass (typically found on the nightside) swap from the ascending track to the
 334 descending track. This is evidenced both in the IRI and in the SLIDEM product, and it can be
 335 seen that SLIDEM performs reasonably well at reproducing the effective ion mass at different
 336 local times.

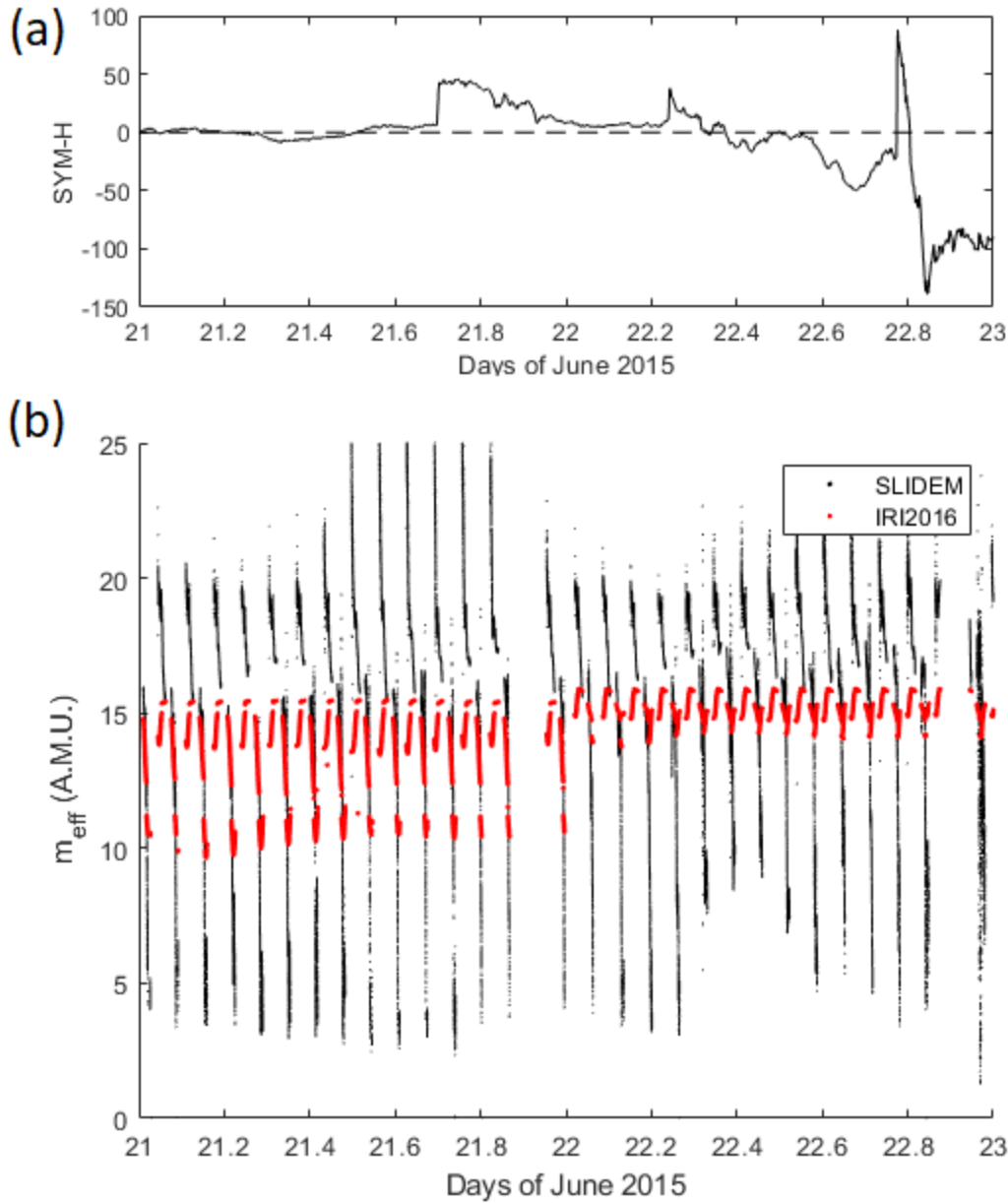


337

338 Figure 4: Year-long plot of effective ion mass for Swarm A for the year 2018, for IRI-2016 (a) and SLIDEM (b). The colorbar is
 339 inverted, i.e. red colours denote periods of lower effective ion mass. The y-axis is quasi-dipole latitude. The dashed lines
 340 delineate the periods of validity, since significant along-track ion drifts are expected to be present at higher latitudes.

341

342 Further analysis shows that SLIDEM is responsive to changes in space weather associated with variations
343 in ion composition. Effective ion mass measurements for the 22 June 2015 storm (Tu et al., 2019) as
344 obtained by SLIDEM (Figure 5 (b), black) show significant changes in nightside effective ion mass on the
345 timescale of hours, e.g. around day 22.4 in June 2015, suggestive of additional O⁺ on the nightside (e.g.
346 Kislser et al., 2015). These changes are captured by IRI-2016 (Figure 5 (b), red) but as that model is
347 parametrized by daily input parameters, the effective ion mass for IRI-2016 changes abruptly around the
348 diurnal change line, which is not physically accurate. In this sense, SLIDEM provides superior estimates
349 of effective ion mass than IRI-2016 during intense geomagnetic storms.



350

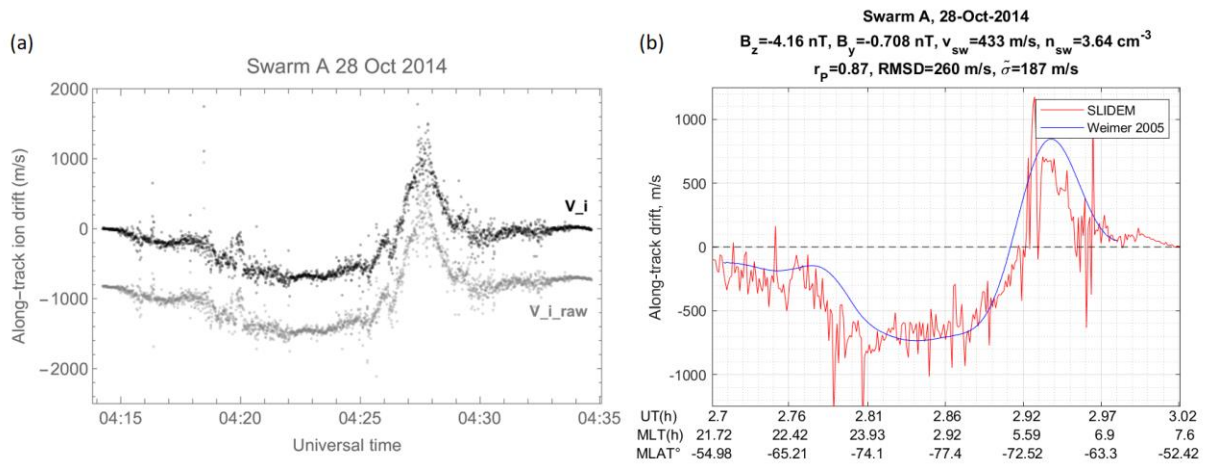
351 Figure 5: a plot of the SYM-H (a) as well as Swarm A IRI-2016 and SLIDEM M_{eff} estimates for the time around the 22 June
 352 2015 storm, denoting the change in effective ion mass during this active time period. In this plot, M_{eff} estimates outside of
 353 the validity range of this parameter (i.e. at high latitudes) are omitted both for SLIDEM and for IRI-2016.

354 **Ion velocity**

355 In Figure 6 (a) plots are along-track ion drift estimates for auroral zone crossings on 28 Oct
 356 2014. The direct output of the SLIDEM algorithm, obtained using equation (10), is shown in the
 357 light-gray points. Variability of order 1 km/s is evident, with respect to random errors
 358 (measurement resolution) of much less than 100 m/s. The systematic flow towards the satellite
 359 is interpreted as the measurement accuracy (~ 0.8 km/s). Detrending the resulting drift, using

360 the method applied to cross-track TII calibration (Burchill and Knudsen, 2020), allows to capture
 361 the correct range of the drift during the auroral crossing, while ensuring it is around zero at
 362 lower latitude. The resulting detrended drift time series (black points) clearly show significant
 363 drift-related disturbances of geophysical origin at high latitudes, with drift settling down at mid-
 364 latitudes.

365 Figure 6 (b) shows an example time series plot of an auroral zone crossing with such SLIDEM
 366 estimates of ion velocity, downsampled to 0.25 Hz (red). Output from the Weimer 2005 electric
 367 field model, obtained following to Lomidze et al. (2019), is plotted in blue. At large scales the
 368 data exhibits near perfect agreement with the model, correctly capturing drift dynamics
 369 including reversals at the right times. Smaller-scale signal is present on top of the large-scale
 370 convection, suggestive of large-magnitude, small-scale Alfvén waves embedded within the
 371 large-scale FACs (e.g. Rother et al., 2007, Pakhotin et al. 2018, 2020).

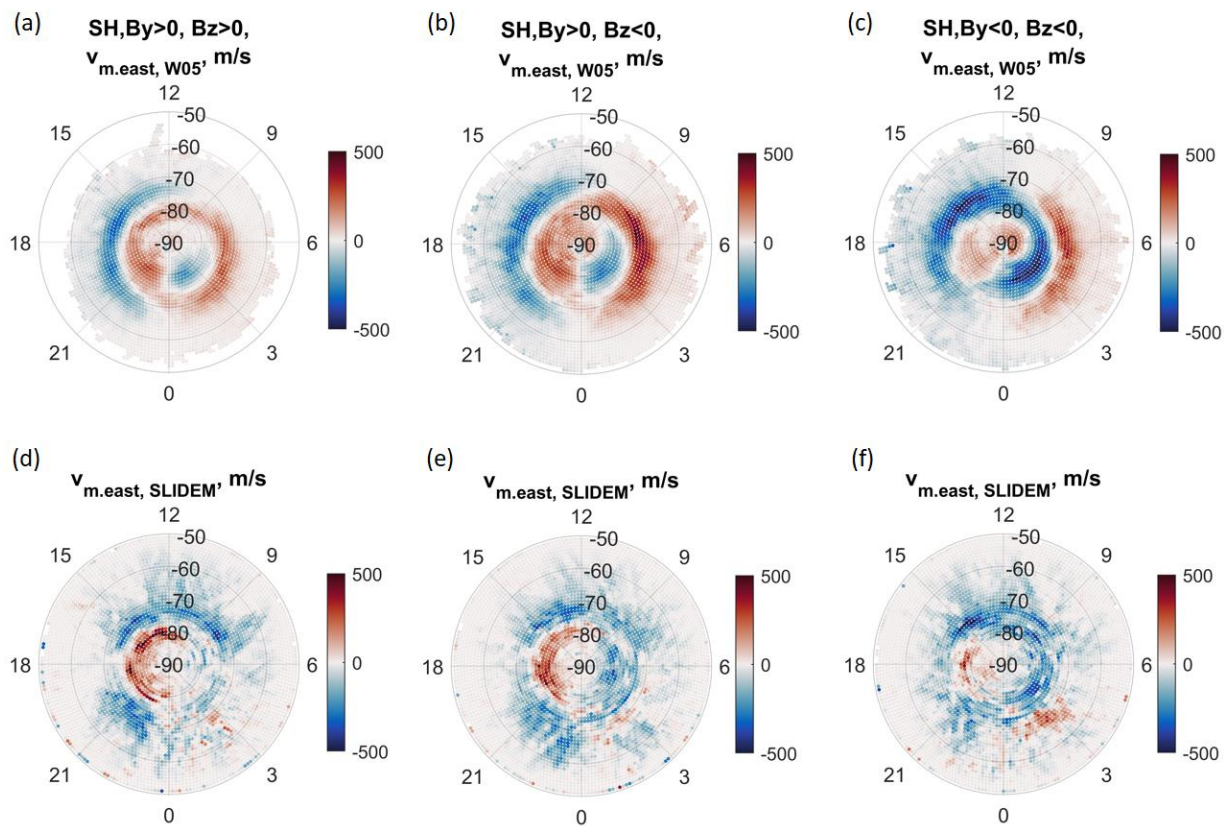


372

373 **Figure 6:** for a representative auroral zone crossing, (a) shows along-track drift estimation using the SLIDEM methodology
 374 using various methods. The gray plot in (a) shows the along-track ion velocity estimate derived using equation (10), where
 375 effective ion mass has been estimated using IRI-2016. Meanwhile the black plot shows the detrended version of the gray
 376 plot, to normalize it such that ion drift at low latitudes is around zero. Panel (b) shows a different auroral zone crossing on
 377 the same day, with the SLIDEM ion velocity output (red) alongside Weimer 2005 ion drift estimations (blue).

378 To further evaluate the validity of ion drifts, following the same methodology as Lomidze et al.
 379 (2019), statistical maps of SLIDEM along-track drift data, obtained by calculating median
 380 components of drifts as a function of magnetic latitude and local time, were created and
 381 compared with corresponding Weimer 2005 model drifts. Polar plots of the magnetic eastward
 382 projection of along-track drift are displayed in Figure 7 for Swarm A in the southern
 383 hemisphere. The SLIDEM product captures some of the topology associated with the high-
 384 latitude ion convection, as well as its dependence on the direction of the IMF. For IMF $B_y > 0$
 385 condition (left and middle panels of Figure 7) both the SLIDEM and Weimer (2005) data show
 386 eastward (positive) flows around -80° and westward (negative) flows around -70° in the post-

387 noon sector. For $B_y < 0$ conditions (right panel in Figure 7) the overall agreement is also
 388 reasonably good poleward of $\sim -70^\circ$. Furthermore, the B_y -dependent asymmetry, i.e., change
 389 from predominantly westward to eastward flows poleward of 70° as B_y changes from positive
 390 to negative (left and middle panels vs right panel in Figure 7) is evident from Weimer 2005
 391 model and well reproduced by the SLIDEM data. The consistency, however, is generally poor for
 392 the dawn sector around -70° , where Weimer 2005 shows eastward flows, while the SLIDEM
 393 shows only the reduced westward drifts. The ion convection typically becomes more intense
 394 when the IMF is southward as indicated by the Weimer model. The corresponding pattern
 395 seems to be largely missing from the SLIDEM data in Figure 7, however a clear pattern appears
 396 in the northward ion drift component (not shown). Part of the noted discrepancies are possibly
 397 due to baseline/bias issues in the SLIDEM. Others indicate certain limitations of the data and
 398 thus provides opportunity for their further refinement.

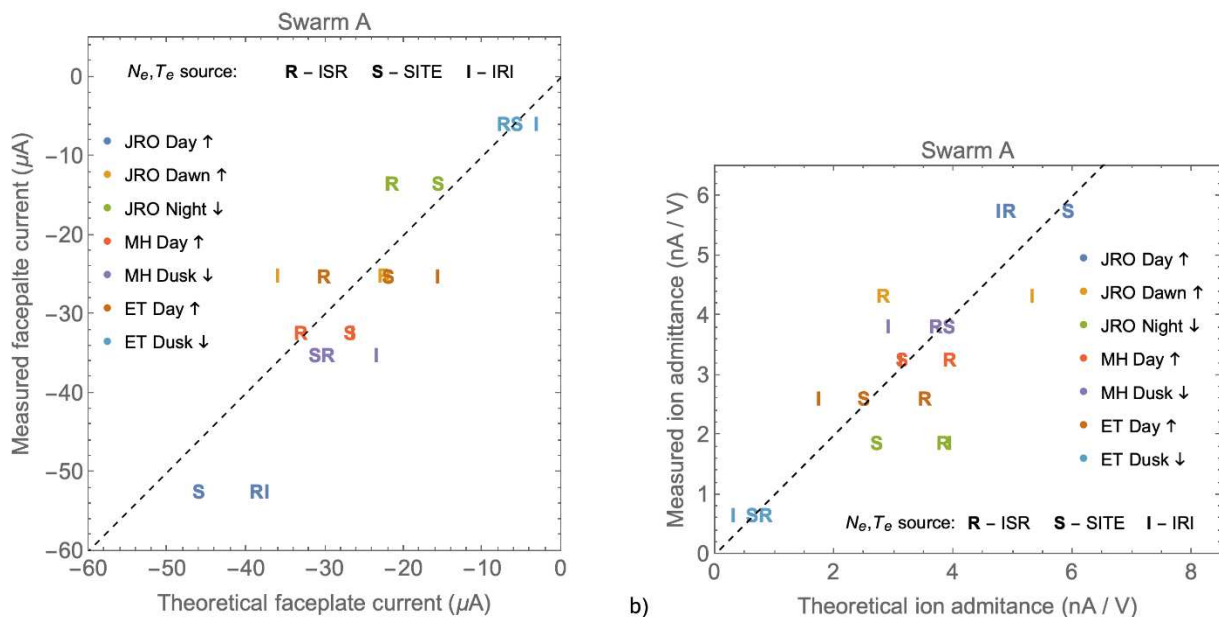


399
 400 **Figure 7: Magnetic latitude-local time maps for Swarm A magnetic eastward ion drift components obtained from along-track**
 401 **data for different IMF conditions in the southern hemisphere. Southward IMF B_z , positive IMF B_y results are shown in (a) for**
 402 **Weimer (2005) and in (d) for SLIDEM. For southward IMF B_z and positive IMF B_y , Weimer 2005 is shown in (b) while SLIDEM**
 403 **is shown in (e). The case of southward IMF B_z and negative IMF B_y is shown in (c) for Weimer (2005) and in (f) for SLIDEM.**

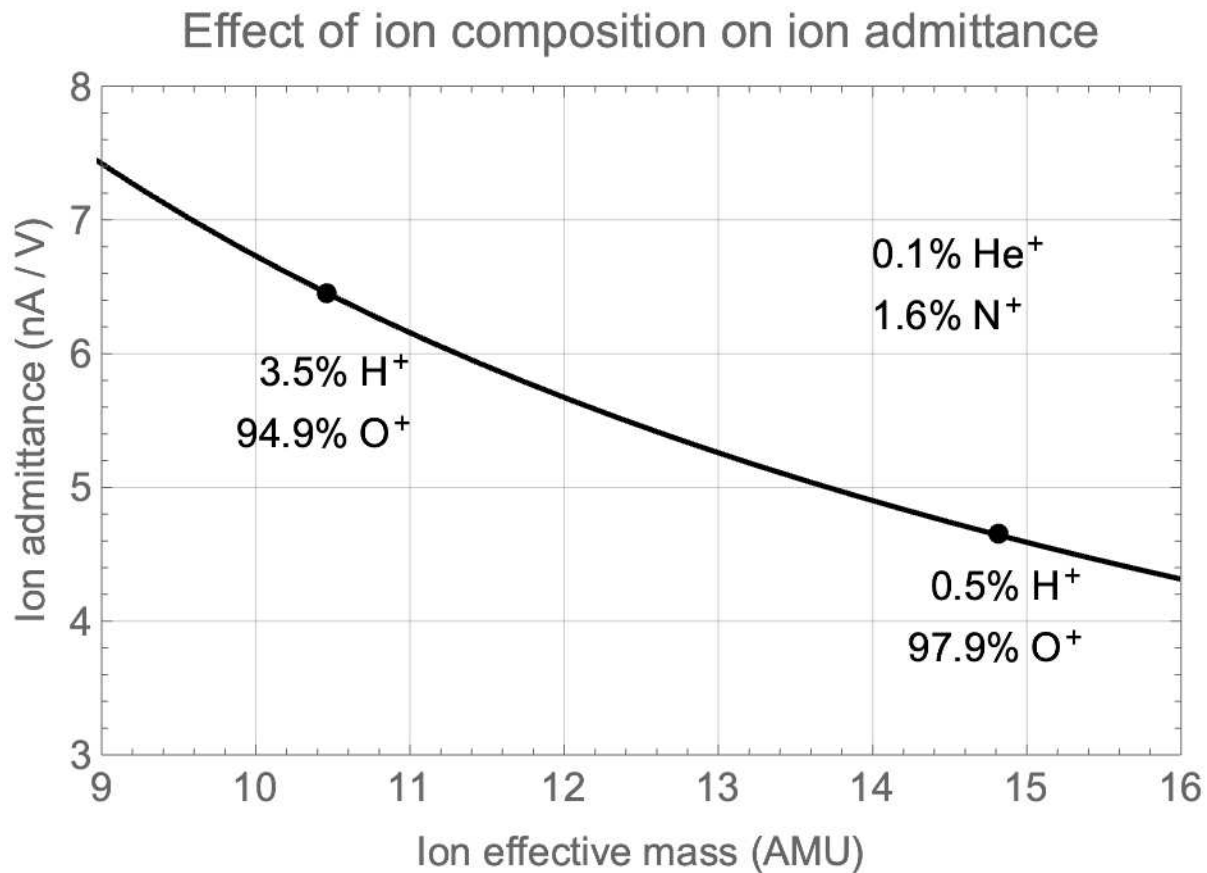
404 **Incoherent scatter radar overflights**

405 For the ground-spacecraft conjunctions, theoretical values for faceplate current and admittance were
 406 calculated using the SLIDEM methodology, using inputs from the radar measurements, from Swarm A,
 407 and from IRI-2016. They were then compared with actual observed current and admittance
 408 measurements. Figure 8 shows the faceplate current (a) and ion admittance (b) measurements from
 409 Swarm A versus theoretical values calculated from radar (R), Swarm SITE (S), and IRI (I) estimates of
 410 electron density and temperature. Colours indicated the radar overflown (JRO – Jicamarca; MH –
 411 Millstone Hill; ET – EISCAT Tromso) and the part of the orbit (day, night, dawn, or dusk, and whether the
 412 satellite was ascending or descending in latitude). Both faceplate current and ion admittance follow the
 413 expected linear trend yet exhibit a significant amount of scatter. The significant scatter in the faceplate
 414 currents arise predominantly from large differences in estimated electron density between the radar,
 415 Swarm, and IRI model. The Swarm faceplate measurements are generally explained best by the in-situ
 416 density (SITE).

417 A significant amount of scatter may be expected particularly in the ion admittance due to small
 418 variations in the concentration of light ions. To illustrate this, Figure 9 shows the theoretical empirically
 419 adjusted ion admittance as a function of effective ion mass for the dayside ascending Jicamarca
 420 overflight using the radar density and temperature estimates. The point at upper right is the theoretical
 421 admittance for the Swarm A dayside ascending overflight of the Jicamarca incoherent scatter radar
 422 facility, using the radar estimates for electron density and temperature and IRI estimates for ion
 423 composition. An increase to 3.5% H+ with concomitant decrease to 94.9% O+ (lower left point)
 424 decreases the expected ion admittance by almost 2 nA/V.



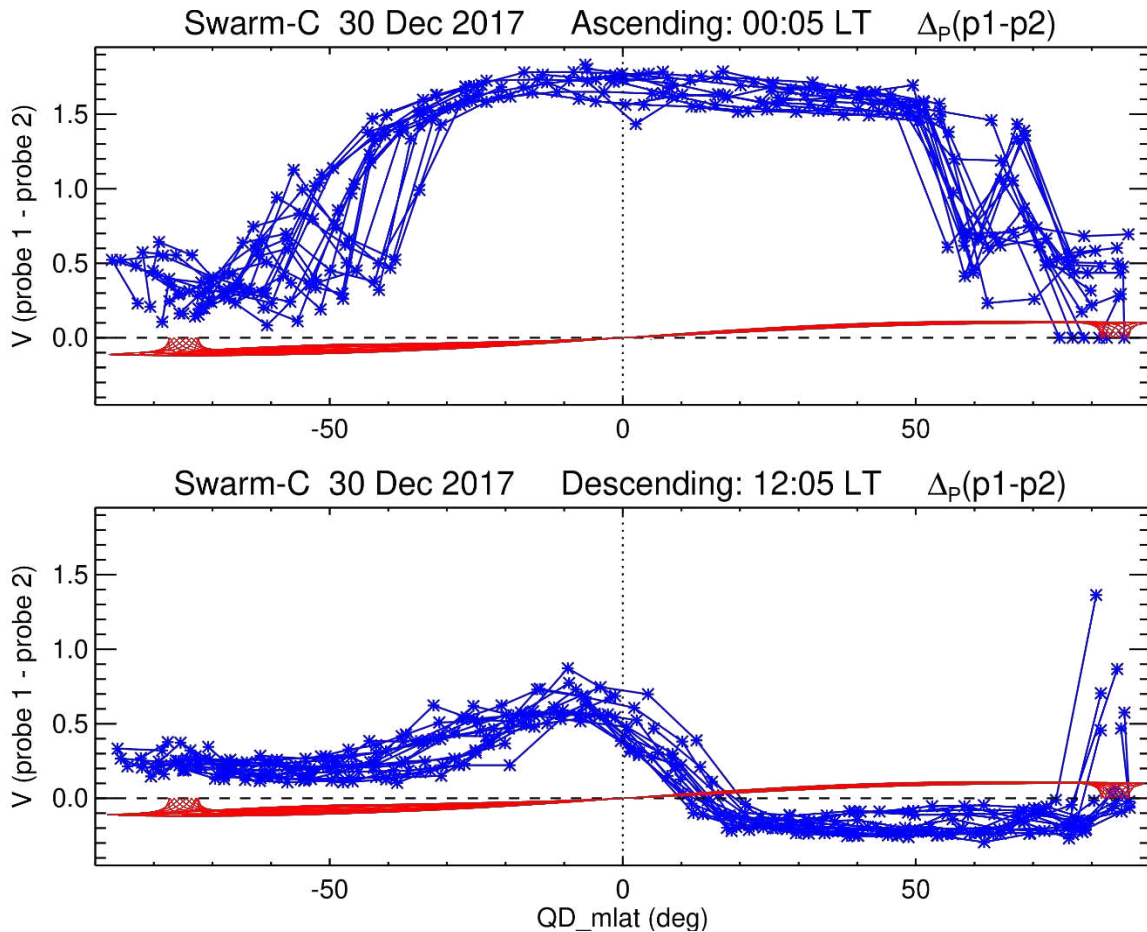
425 a) 426 **Figure 8: Incoherent scatter radar facility validation. a) Measured faceplate current versus theoretical current for each radar**
 427 **facility and for each of three estimates used for electron density and temperature. Ion composition was estimated using the**
 428 **IRI in all cases. b) Measured versus theoretical ion admittance. Theoretical values include adjustments based on PIC**
 429 **simulations from Resendiz Lira et al. (2019) and Resendiz Lira and Marchand (2021).**



431

432 **Figure 9: Illustration of the large sensitivity of ion admittance to small variations in light ion composition. The point at lower**
 433 **right is the theoretical admittance for the Swarm A dayside ascending overflight of the Jicamarca incoherent scatter radar**
 434 **facility, using the radar estimates for electron density and temperature and IRI estimates for ion composition. An increase to**
 435 **3.5% H⁺ with concomitant decrease to 94.9% O⁺ (upper left point) decreases the ion admittance by almost 2 nA/V.**

436 The spacecraft floating potential – which enters into several of the SLIDEM equations – is
 437 obtained from the Langmuir probes, as an average between the low-gain and high-gain probe.
 438 Figure 10 shows one day of data records (~16 orbits) of the floating potential differences
 439 between the two Langmuir probes as a function of QD latitude (blue curve). The two potentials
 440 usually disagree, sometimes by more than 1.5 V, a value much larger than the potential
 441 difference associated with e.m.f. from motion of the satellite through the geomagnetic field
 442 (red curve). The observations suggest the presence of strong electric fields in the vicinity of the
 443 EFI, or an issue with the calibration of the potential estimates, as well as the fact the two
 444 probes are made of different materials. The SLIDEM products are flagged for cases when the
 445 two probe estimates for floating potential differ by more than 0.3 V.



446

447 Figure 10: an example of the difference of floating potential estimates between Langmuir probes 1 and 2 (blue) as a function
 448 of QD_Mlat, for nightside (ascending, top) and dayside orbits (descending, bottom). The red plot shows the theoretical inter-
 449 probe potential variation which may be expected as a result of electro-magnetic forces created by the spacecraft's motion.

450

451 4. Discussion

452 The SLIDEM methodology aims to estimate three parameters using Swarm data: density,
 453 effective ion mass, and along-track ion drift. In the process it also estimates the plasma sheath
 454 effects of the faceplate and Langmuir probe and the local Debye length, but these parameters
 455 are not investigated in this paper. For the three primary parameters of interest, the
 456 methodology broadly performs as expected.

457 The primary advantage of density estimations using SLIDEM over existing Swarm L1b LP data is
 458 its ability to take into account the changes in ion composition in the topside and removal of
 459 non-zero ion drift assumption at high latitudes. Our analysis based on January 2018 data yields
 460 better agreement with IRI-2016 (Figures 1, 2), particularly on the nightside where light ions
 461 significantly change effective ion mass from the generally assumed 16 AMU. Similar to Bilitza
 462 and Xiong (2021) who showed -42% percentage deviation compared to other measurements,

463 our results also show that the IRI overestimates densities in the topside ionosphere. Overall
464 difference between the two Swarm products is smaller than that with IRI, however assuming IRI
465 better captures density variation related to the light ions, the smaller difference between the
466 SLIDEM and IRI at night could indicate an advantage of the new data product.

467 Our results showed the SLIDEM values tend to be lower than those by Swarm LP on the
468 nightside. Previous analysis of Swarm LP data (Lomidze et al., 2018, 2021; Larson et al., 2021),
469 however, demonstrated that overall the Swarm data are 20-35 % lower than those by other
470 independent measurements. In those studies, coincident data from ISRs, ionosondes, and radio
471 occultation were used, and all latitudes and local times were covered. The analysis of Swarm LP
472 data at lower and middle latitudes during nighttime was part of the Lomidze et al. (2018) study
473 who found ~4-12 % lower Swarm densities (equivalent to 2-6 % lower plasma frequencies) than
474 those by the COSMIC radio occultation, thus the difference was smaller (less underestimation)
475 than the overall trend. Also note that the period considered in that study (December 2013-June
476 2016) is characterized by a higher solar activity than January 2018 (considered for SLIDEM). The
477 composition of light ions, furthermore, is known to be more significant at a given altitude in the
478 topside for lower solar activity conditions at night. In order to better evaluate the performance
479 of SLIDEM density, and understand how the low latitude, nighttime Swarm LP density accuracy
480 varies compared to independent measurements as solar activity changes from high to low, it is
481 important to extend the corresponding analyses to the entire Swarm mission in a future study.

482 For effective ion mass estimations, SLIDEM estimations correctly capture M_{eff} variations both
483 as a result of orbital dynamics (Figures 3, 4) and space weather (Figure 5). The disagreement on
484 the timing of the change in M_{eff} (Figure 5) may likely be due to IRI-2016 not capturing the
485 time-delayed chain of events which occur during a geomagnetic storm. Indeed, the model
486 outputs instant values when initialized with a set of parameters. Meanwhile, a real
487 magnetosphere has memory and information about what has happened in the past is necessary
488 to correctly predict future behavior during rapidly changing geomagnetic conditions.

489 For along-track ion velocity estimation, (Figure 6 (b)), the employed scheme is capable of
490 producing realistic ion velocity drifts which can be in good agreement with Weimer (2005)
491 model estimates, capturing both the correct magnitudes as well as the large-scale structure.
492 Smaller-scale structures superimposed on the large-scale drifts is likely indicative of large-
493 magnitude Alfvén waves.

494 Climatology obtained using the SLIDEM drifts are capable of reproducing some of the main
495 features of the high-latitude convection, in agreement with Weimer 2005. In particular, the
496 westward drifts in the post-noon equatorward sector and the eastward drifts in the poleward
497 noon sector, as well as the IMF B_y -dependent asymmetry and IMF B_z -dependent flow
498 enhancements (for the northward drifts). Certain features, e.g. the eastward drifts in the

499 equatorward morning sector and enhanced zonal drifts with southward IMF are not well-
500 reproduced, and further analysis is needed. Overall, comparison results also imply the general
501 level of accuracy of the ion drift attained, being of the order of several hundred m/s.
502 Furthermore, the fact that the SLIDEM drifts are often of very small in magnitude equatorward
503 of -60 degrees is an indication of the effectiveness of the post-processing linear detrending. In
504 general, the product would benefit from further refinement to remove sources of uncertainty
505 and investigate the effects of Langmuir probe plasma sheath effects more rigorously.
506 Nevertheless, it is capable of producing reasonable agreement with independent model
507 estimates and it may be possible to use SLIDEM along-track estimates to improve the quality of
508 the TII along-track ion velocity estimations which currently suffer from known issues (Knudsen
509 et al., 2017, Koustov et al., 2019).

510 A brief discussion of potential sources of uncertainty will follow. These present potential error
511 sources which may be responsible for disagreement between SLIDEM products and
512 independent estimates, particularly with along-track ion drift estimations.

513 Photoelectron effects refer to those electrons emitted as a result of solar irradiation of the
514 satellite. Resendiz Lira et al. (2019) argue that these may be safely neglected on the nightside,
515 and in areas of high density where collected ion currents exceed those from photoelectron
516 emission. As a result, they do not appear in the faceplate nor the Langmuir probe effective area
517 correction terms.

518 The geomagnetic field may be positioned in such a way that the Swarm body shields the
519 Langmuir probe from incoming field-aligned electrons, whose small gyroradii mean they impact
520 the satellite before the probe. If true, this effect should be observed on one hemisphere but
521 not on the other, since the magnetic field will be 'disconnected' from the Langmuir probe on
522 one side of the equator and 'connected' on the other from the magnetosphere side. There is
523 some evidence of a small interhemispheric change in effective ion mass estimates (see e.g.
524 Figure 3) which may be due to this effect, and it is worth exploring further. Nevertheless, it is
525 not believed to be large enough to account for significant differences between simulated and
526 measured admittance values. It should be noted that SLIDEM utilizes the ion admittance
527 measurements (negative probe bias), and thus the admittance is not expected to be directly
528 impacted by aforementioned electron dynamics.

529 Finally, the aforementioned ambiguities in spacecraft floating potential estimates, which often
530 vary between the two probes, present a further potential error source, since this parameter
531 enters into equations (8) and (9) and thus affects the extent of the plasma sheath effects.

532 **5. Conclusions**

533 A new plasma density, effective ion mass and along-track ion velocity product has been
534 developed, following OML methodology and relaxing the assumptions present in the existing
535 Level 1b Swarm density estimation method. The new density data product has been validated
536 through comparison with empirical models. A significant finding is that for the month-long
537 period analyzed, the revised ion density estimate has consistently lower residuals with respect
538 to IRI ion density, particularly on the nightside, when compared with the Level 1b methodology,
539 due to improved estimation of the effective ion mass which deviates significantly from 16 AMU
540 when light ions are present. The effective ion mass estimations have also been compared with
541 IRI and have been found to exhibit good agreement in longer, year-long comparison,
542 reproducing changes in effective ion mass associated with space weather as well as due to
543 Swarm orbital drift.

544 For along-track ion velocity, the data product was compared with the Weimer 2005 electric
545 field model. Cases with good agreement were found for individual passes, while statistical
546 analysis following Lomidze et al. (2019) demonstrated reasonable agreement reproducing some
547 major features of global ion convection related to latitude, local time, and IMF variation. It is
548 found that detrending the flows following the method used for TII cross-track ion velocities
549 (Burchill and Knudsen, 2020) is required. The future improvements in the data quality are
550 needed to address some of the caveats that were found from the analysis.

551 A historical dataset, PREL 0101, has been generated covering the same interval as the Swarm
552 EXTENDED_LP_FP dataset (2 October 2014 through 18 October 2021). Data quality flagging is at an
553 early stage of development; users are encouraged to read the SLIDEM Product Description
554 Document (Pakhotin and Burchill, 2021). It is anticipated that this dataset will facilitate new
555 scientific investigations in ionospheric physics and space weather as well as investigations into
556 the Swarm TII ion drift and LP ion density data quality.

557 **6. Declarations**

558 **Availability of data and materials**

559 Swarm data are available from ESA at <http://swarm-diss.eo.esa.int>. The IDL software for the
560 Weimer 2005 model is available in the Zenodo repository (at
561 <http://doi.org/10.5281/zenodo.2530324>). Millstone Hill, Jicamarca, and EISCAT-Tromso
562 incoherent scatter radar data were obtained from the Madrigal database at
563 <http://www.openmadrigal.org/>.

564 **Competing Interests**

565 The authors declare that they have no competing interests.

566 **Funding**

567 IPP was supported by the European Space Agency Swarm DISC SLIDEM contract. JKB was
568 supported by funding from the Canadian Space Agency.

569 **Authors' Contributions**

570 JB and MF created and developed the concept including the mathematical foundations of the
571 methodology, and performed preliminary analysis using Swarm and IRI-2016 data. IPP was
572 mainly responsible with performing the analysis to quality SLIDEM data against IRI-2016,
573 curating the conjunction list, and writing the manuscript. LL performed analysis of SLIDEM
574 along-track ion drift estimates and operated the Weimer 2005 model to create the statistical
575 and case study comparisons between the empirical model and the observations. All authors
576 read and approved the final manuscript.

577 **Acknowledgements**

578 Prof. Richard Marchand (University of Alberta) provided feedback on a draft of this paper.

579 **7. References**

580 Appleton, E. Two Anomalies in the Ionosphere. *Nature* 157, 691 (1946).

581 <https://doi.org/10.1038/157691a0>

582 Archer, W. E., Knudsen, D. J., Burchill, J. K., Jackel, B., Donovan, E., Connors, M., et al. (2017).
583 Birkeland current boundary flows. *Journal of Geophysical Research: Space Physics*, 122, 4617–
584 4627. <https://doi.org/10.1002/2016JA023789>

585 Balan, N., & Bailey, G. J. (1995). Equatorial plasma fountain and its effects: Possibility of an
586 additional layer, *Journal of Geophysical Research*, 100, 21421–21432.

587 <https://doi.org/10.1029/95JA01555>

588 Bilitza, D., D. Altadill, V. Truhlik, V. Shubin, I. Galkin, B. Reinisch, and X. Huang (2017),
589 International Reference Ionosphere 2016: From ionospheric climate to real-time weather
590 predictions, *Space Weather*, 15, 418–429, doi:10.1002/2016SW001593.

591 Bilitza, D. and Xiong, C. (2021), A solar activity correction term for the IRI topside electron
592 density model, *Advances in Space Research*, 68, 2124–2137,
593 <https://doi.org/10.1016/j.asr.2020.11.012>.

594 Buchert, S. (2015), EFI LP Preliminary Data Release Notes, Swarm Expert Support Laboratories
595 (Technical Report). Report No. SW-RN-IRF-GS-002, Rev: 1, 2015-0206 (European Space Agency,
596 2015).

597 Burchill, J. & Knudsen, D. J. EFI TII Cross-Track Flow Data Release Notes, Swarm Data,
598 Innovation, and Science Cluster (Technical Report). Report No. SW-RN-UoC-GS-004, Rev. 5
599 (European Space Agency, 2020).

600 Codrescu, M. V., T. J. Fuller-Rowell, and J. C. Foster (1995), On the importance of E-field
601 variability for Joule heating in the high-latitude thermosphere, *Geophys. Res. Lett.*, 22(17), 2393
602 – 2396

603 Evans, J. V. (1969). Theory and practice of ionosphere study by Thomson scatter radar.
604 *Proceedings of the IEEE*, 57(4), 496–530. <https://doi.org/10.1109/PROC.1969.7005>

605 Friis-Christensen, E., Luhr, H., Knudsen, D., & Haagmans, R. (2008). Swarm—An Earth
606 observation mission investigating geospace. *Advances in Space Research*, 41(1), 210–216.
607 <https://doi.org/10.1016/j.asr.2006.10.008>

608 Ganushkina, N. Y., Liemohn, M. W., Dubyagin, S., Daglis, I. A., Dandouras, I., De Zeeuw, D. L.,
609 Ebihara, Y., Ilie, R., Katus, R., Kubyshkina, M., Milan, S. E., Ohtani, S., Ostgaard, N., Reistad, J. P.,
610 Tenfjord, P., Toffoletto, F., Zaharia, S., and Amariutei, O.: Defining and resolving current
611 systems in geospace, *Ann. Geophys.*, 33, 1369–1402, [https://doi.org/10.5194/angeo-33-1369-](https://doi.org/10.5194/angeo-33-1369-2015)
612 2015, 2015.

613 Greenwald RA, Baker KB, Dudeney JR, Pinnock M, Jones TB, Thomas EC, Villain J-P, Cerisier J-C,
614 Senior C, Hanuise C, Hunsucker RD, Sofko G, Koehler J, Nielsen E, Pellinen R, Walker ADM, Sato
615 N, Yamagishi H (1995), DARN/SuperDARN: a global view of the dynamics of high-latitude
616 convection. *Space Sci Rev* 71:761–796

617 Jørgensen, J. L., Friis-Christensen, E., Brauer, P., Primdahl, F., Jørgensen, P. S., Allin, T. H., &
618 Denver, T. (2008). The Swarm magnetometry package. In *Small satellites for Earth observation*
619 (pp. 143-151). Springer, Dordrecht.

620 Kistler, L. M., et al. (2016), The source of O⁺ in the storm time ring current, *J. Geophys. Res.*
621 *Space Physics*, 121, 5333–5349, doi:10.1002/2015JA022204.

622 Knudsen, D. J., Burchill, J. K., Buchert, S. C., Eriksson, A. I., Gill, R., Wahlund, J. E., et al. (2017).
623 Thermal ion imagers and Langmuir probes in the Swarm electric field instruments. *Journal of*
624 *Geophysical Research: Space Physics*, 122, 2655–2673. <https://doi.org/10.1002/2016JA022571>

625 Koustov, A. V. et al. (2019). A comparison of cross-track ion drift measured by the Swarm
626 satellites and plasma convection velocity measured by SuperDARN. *J. Geophys. Res. Space Phys.*
627 124, 4710–4724.

628 Larson, B., Koustov, A. V., Kouznetsov, A. F., Lomidze, L., Gillies, R. G., & Reimer, A. S. (2021). A
629 comparison of the topside electron density measured by the Swarm satellites and incoherent
630 scatter radars over Resolute Bay, Canada. *Radio Science*, 56, e2021RS007326.
631 <https://doi.org/10.1029/2021RS007326>

632 Lomidze, L., Knudsen, D. J., Burchill, J., Kouznetsov, A., & Buchert, S. C. (2018). Calibration and
633 validation of Swarm plasma densities and electron temperatures using ground-based radars
634 and satellite radio occultation measurements. *Radio Science*, 53, 15–36.
635 <https://doi.org/10.1002/2017RS006415>

636 Lomidze, L., Burchill, J. K., Knudsen, D. J., Kouznetsov, A., & Weimer, D. R. (2019). Validity study
637 of the Swarm horizontal cross-track ion drift velocities in the high-latitude ionosphere. *Earth
638 and Space Science*, 6, 411–432. <https://doi.org/10.1029/2018EA000546>

639 Lomidze, L., Burchill, J. K., Knudsen, D. J., & Huba, J. D. (2021). Estimation of ion temperature in
640 the upper ionosphere along the Swarm satellite orbits. *Earth and Space Science*, 8,
641 e2021EA001925. <https://doi.org/10.1029/2021EA001925>

642 R. Marchand. (2012). Ptetra, a tool to simulate low orbit satellite–plasma interaction. *IEEE
643 Transactions on Plasma Science*, 40(2):217–229.

644 Mott-Smith, H. M., and I. Langmuir (1926), “The Theory of Collectors in Gaseous Discharges”,
645 *Phys. Reviews*, 28, 727, 1926.

646 Pakhotin, I. P., Mann, I. R., Lysak, R. L., Knudsen, D. J., Gjerloev, J. W., Rae, I. J., et al. (2018).
647 Diagnosing the role of Alfvén waves in Magnetosphere-ionosphere coupling: Swarm
648 observations of large amplitude nonstationary magnetic perturbations during an interval of
649 northward IMF. *Journal of Geophysical Research: Space Physics*, 123, 326–340.
650 <https://doi.org/10.1002/2017JA024713>

651 Pakhotin, I. P., Mann, I. R., Knudsen, D. J., Lysak, R. L., & Burchill, J. K. (2020). Diagnosing the
652 role of Alfvén waves in global field-aligned current system dynamics during southward IMF:
653 swarm observations. *Journal of Geophysical Research: Space Physics*, 125, e2019JA027277.
654 <https://doi.org/10.1029/2019JA027277>

655 Pakhotin, I.P., Mann, I.R., Xie, K. et al. (2021). Northern preference for terrestrial
656 electromagnetic energy input from space weather. *Nat Commun* 12, 199 (2021).
657 <https://doi.org/10.1038/s41467-020-20450-3>

658 Pakhotin and Burchill (2021), Swarm LP Ion Drift and Effective Mass Product Definition, Swarm
659 Data, Innovation, and Science Cluster (Technical Report). Report no.: SW-TN-UoC-GS-001: 1dA,
660 30 Aug 2021 (European Space Agency, 2021).

661 Park, J., H. Lühr, C. Stolle, J. Rodriguez-Zuluaga, D. J. Knudsen, J. K. Burchill, and Y.-S. Kwak
662 (2016), Statistical survey of nighttime midlatitude magnetic fluctuations: Their source location
663 and Poynting flux as derived from the Swarm constellation, *J. Geophys. Res. Space Physics*, 121,
664 11,235–11,248, doi:10.1002/2016JA023408.

665 Resendiz Lira, P. A., Marchand, R., Burchill, J., & Förster, M. (2019). Determination of swarm
666 front plate's effective cross section from kinetic simulations. *IEEE Transactions on Plasma
667 Science*, 47(8), 3667–3672.

668 Resendiz Lira, P. A., & Marchand, R. (2021). Simulation inference of plasma parameters from
669 Langmuir probe measurements. *Earth and Space Science*, 8, e2020EA001344.
670 <https://doi.org/10.1029/2020EA001344>

671 Rother, M., Schlegel, K., & Lühr, H. (2007). CHAMP observation of intense kilometer-scale field
672 aligned currents, evidence for an ionospheric Alfvén resonator. *Annales Geophysicae*, 25(7),
673 1603–1615. <https://doi.org/10.5194/angeo-25-1603-2007>

674 Smirnov, A., Shprits, Y., Zhelavskaya, I., Lühr, H., Xiong, C., Goss, A., et al. (2021).
675 Intercalibration of the plasma density measurements in Earth's topside ionosphere. *Journal of
676 Geophysical Research: Space Physics*, 126, e2021JA029334.
677 <https://doi.org/10.1029/2021JA029334>

678 Truhlik, V., D. Bilitza, and L. Tříšková (2015), Towards better description of solar activity
679 variations in IRI ion composition model, *Adv. Space Res.*, 55(8), 2099–2105,
680 doi:10.1016/j.asr.2014.07.033.

681 Tu, W., Xiang, Z., & Morley, S. K. (2019). Modeling the magnetopause shadowing loss during the
682 June 2015 dropout event. *Geophysical Research Letters*, 46, 9388–9396.
683 <https://doi.org/10.1029/2019GL084419>

684 Verkhoglyadova, O. P., X. Meng, A. J. Mannucci, M. G. Mlynczak, L. A. Hunt, and G. Lu (2017),
685 Ionosphere-thermosphere energy budgets for the ICME storms of March 2013 and 2015
686 estimated with GITM and observational proxies, *Space Weather*, 15, 1102–1124,
687 doi:10.1002/2017SW001650.

688 Verkhoglyadova, O. P., Meng, X., Mannucci, A. J., & McGranaghan, R. M. (2018). Semianalytical
689 estimation of energy deposition in the ionosphere by monochromatic Alfvén waves. *Journal of
690 Geophysical Research: Space Physics*, 123, 5210–5222. <https://doi.org/10.1029/2017JA025097>

691 Weimer, D. R. (2005). Improved ionospheric electrodynamic models and application to
692 calculating Joule heating rates. *Journal of Geophysical Research*, 110, A05306.
693 <https://doi.org/10.1029/2004JA010884>

694 Woodman, R. F. & La Hoz (1976). C. Radar observations of F region equatorial irregularities. J.
695 Geophys. Res. 81, 5447–5466.

696 Yamazaki, Y.; Maute, A. (2017). Sq and EEJ—A review on the daily variation of the geomagnetic field
697 caused by ionospheric dynamo currents. Space Sci. Rev. 2017, 206, 299–405

698 **Appendix A**

699 Table of conjunction times between Swarm A and ground stations

Conjunction	Time (UT)
Swarm-A/Jicamarca (dayside)	2017-09-07 15:18
Swarm-A/Jicamarca (nightside)	2019-03-25 00:25
Swarm-A/Jicamarca (nightside)	2015-05-28 06:38
Swarm-A/Millstone Hill (dayside)	2015-04-10 22:33
Swarm-A/Millstone Hill (nightside)	2015-07-16 01:21
Swarm-A/EISCAT-Tromso (dayside)	2015-07-08 08:50
Swarm-A/EISCAT-Tromso (nightside)	2016-01-07 03:33

700

Supplementary Files

This is a list of supplementary files associated with this preprint. Click to download.

- [graphicalAbstract.png](#)